PHYSICAL REVIEW MATERIALS **2**, 011401(R) (2018)

Rapid Communications **Editors' Suggestion**

Magnetic proximity effect in Pt/$CoFe_2O_4$ bilayers

Walid Amamou,[1] Igor V. Pinchuk,[2] Amanda H. Trout,[3,4] Robert E. A. Williams,[3] Nikolas Antolin,[4] Adam Goad,[2,5]
Dante J. O'Hara,[1] Adam S. Ahmed,[2] Wolfgang Windl,[4] David W. McComb,[3,4] and Roland K. Kawakami[1,2,*]
[1]*Materials Science and Engineering, University of California, Riverside, California 92521, USA*
[2]*Department of Physics, The Ohio State University, Columbus, Ohio 43210, USA*
[3]*Center for Electron Microscopy and Analysis, The Ohio State University, Columbus, Ohio 43210, USA*
[4]*Department of Materials Science and Engineering, The Ohio State University, Columbus, Ohio 43210, USA*
[5]*Department of Physics, University of Maryland, Baltimore County, Maryland 21250, USA*

(Received 21 June 2017; published 12 January 2018)

We observe the magnetic proximity effect (MPE) in Pt/$CoFe_2O_4$ bilayers grown by molecular beam epitaxy. This is revealed through angle-dependent magnetoresistance measurements at 5 K, which isolate the contributions of induced ferromagnetism (i.e., anisotropic magnetoresistance) and the spin Hall effect (i.e., the spin Hall magnetoresistance) in the Pt layer. The strong evidence for induced ferromagnetism in Pt via the anisotropic magnetoresistance is supported further by density functional theory calculations and various control measurements including the insertion of a Cu spacer layer to suppress the induced ferromagnetism. In addition, anomalous Hall effect measurements show an out-of-plane magnetic hysteresis loop of the induced ferromagnetic phase with larger coercivity and larger remanence than the bulk $CoFe_2O_4$. By demonstrating the MPE in Pt/$CoFe_2O_4$, these results establish the spinel ferrite family as a promising material for the MPE and spin manipulation via proximity exchange fields.

DOI: 10.1103/PhysRevMaterials.2.011401

Spin manipulation inside a nonmagnetic (NM) material using internal effective fields (spin orbit or exchange) is a very promising avenue toward the realization of next generation spintronic devices (spin transistors, magnetic gates, etc.) [1,2]. In particular, the magnetic proximity effect (MPE) at the interface of a NM spin channel and a ferromagnetic (or ferrimagnetic) insulator (FMI) is of great importance for generating exchange fields and induced ferromagnetism in the NM layer. Recently, spin manipulation by the MPE has been realized in experiments that modulate spin currents in graphene on yttrium iron garnet (YIG) [3,4]. In addition, proximity exchange fields induced by a FMI have been observed for graphene and monolayer transition-metal dichalcogenides [5–7]. The MPE with topological insulators is also of great interest for developing the quantum anomalous Hall effect at room temperature [8,9].

Although the MPE has been achieved using garnets (e.g., YIG and thulium iron garnet [3,4,7,10]) and chalcogenides (e.g., EuS [5,6]) as the FMI, the use of spinel ferrites (MFe_2O_4 with $M =$ Co, Ni, etc.) for the MPE has been notably absent. In fact, attempts to detect the MPE in Pt/$CoFe_2O_4$ (CFO) through transport measurements and element specific x-ray magnetic circular dichroism have drawn the conclusion that there is no MPE induced in the Pt layer [11–15]. This is a substantial limitation for spintronics due to the unusual versatility that the spinel ferrites provide. Unlike chalcogenides, they have Curie temperatures above room temperature and can be magnetically hard (e.g., CFO) or soft (e.g., $Zn_{0.5}Mg_{0.5}Fe_2O_4$). CFO also has large magnetostriction and magnetoelastic coefficients, meaning its magnetic properties can be tuned strongly through epitaxial strain [16–18] and controlled electrically using piezoelectric substrates [19]. Furthermore, magnetoelectric switching has been realized in CFO [20]. Most importantly for spintronic devices, CFO and $NiFe_2O_4$ (NFO) are integrated readily into single-crystalline heterostructures with relevant spintronic materials MgO(001), Fe(001), Cr(001), and others, which have enabled the use of CFO for spin-dependent tunnel barriers ("spin filtering") [21–23], and should make it straightforward to implement electrostatic back gates for gate-tunable MPEs (which is difficult for garnets). Thus, previous reports on the absence of MPEs with CFO and NFO have effectively removed spinel ferrites from the discussion [11–15,24]. However, these studies of the MPE have employed either sputtering or pulsed laser deposition of the spinel ferrite, whereas this work utilizes molecular beam epitaxy (MBE) for the growth.

In this Rapid Communication, we investigate MBE-grown Pt/CFO bilayers and observe induced ferromagnetism (i.e., the MPE) in the Pt layer at 5 K. This is revealed through angle-dependent magnetoresistance (ADMR) measurements, which isolate the contributions of induced ferromagnetism [i.e., anisotropic magnetoresistance (AMR)] and the spin Hall effect [i.e., the spin Hall magnetoresistance (SMR)] in the Pt layer. The strong evidence for induced ferromagnetism in Pt via AMR is supported further by density functional theory (DFT) calculations and various control measurements including the insertion of a Cu spacer layer to suppress the induced ferromagnetism. In addition, the anomalous Hall effect (AHE) measurements show an out-of-plane magnetic hysteresis loop of the induced ferromagnetic phase with larger coercivity and larger remanence than the bulk CFO. By demonstrating a MPE in Pt/CFO, these results establish the spinel ferrite family as

---

[*] kawakami.15@osu.edu

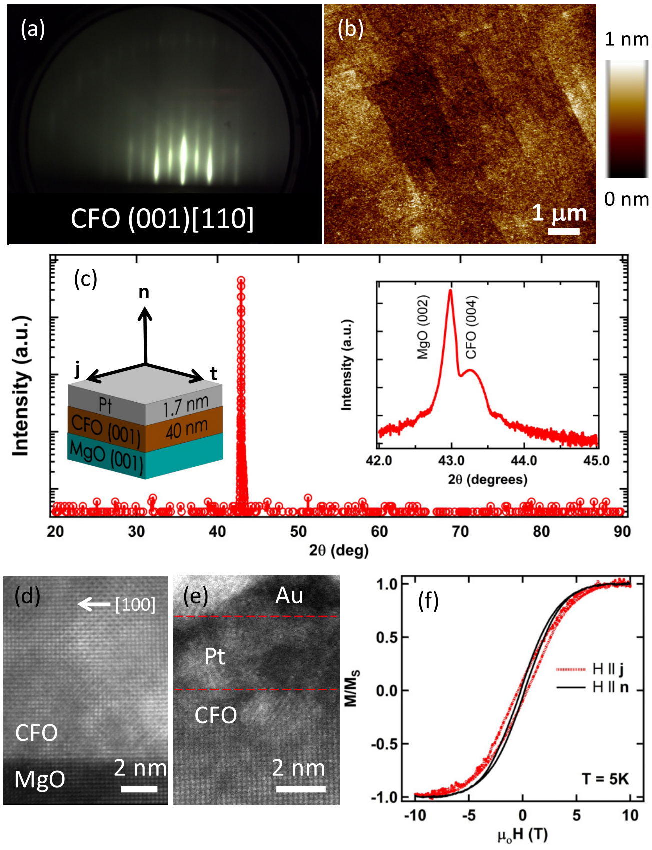

FIG. 1. (a) RHEED image of a 40-nm CFO film grown on a MgO(001) substrate, taken along the [110] in-plane direction. (b) Representative atomic force microscopy image taken over a 10 × 10 μm^2 scan size with rms roughness of 0.14 nm. (c) A θ-2θ x-ray diffraction scan of a Pt(1.7-nm)/CFO(40-nm)/MgO heterostructure. The inset: A fine scan showing a clear CFO(004) peak. (d) and (e) HAADF STEM micrographs of the CFO/MgO interface and Pt/CFO interface, respectively. (f) Magnetic hysteresis loops of Pt(1.7 nm)/CFO(40 nm)/MgO for both in-plane (red dashed line) and out-of-plane (black solid line) applied magnetic fields.

a promising material for the MPE and spin manipulation via proximity exchange fields.

The CFO thin films are grown on MgO(001) substrates by reactive MBE (details in the Supplemental Material [25]) and are characterized by reflection high-energy electron diffraction (RHEED), atomic force microscopy (AFM), x-ray diffraction (XRD), and high angle annular dark-field scanning transmission electron microscopy (HAADF STEM). Figure 1(a) shows a RHEED pattern of CFO(40 nm)/MgO(001) taken along the [110] in-plane direction. The image displays streaky and sharp diffraction maxima, indicating a flat and single-crystal surface. This is confirmed by AFM, which exhibits very smooth morphology over large areas [Fig. 1(b)] with a rms roughness of 0.14 nm over a 10 × 10 μm^2 area of a 40-nm CFO film. The crystallinity is confirmed by θ-2θ XRD scans on Pt(1.7 nm)/CFO(40 nm)/MgO(001), which exhibit clear MgO(002) and CFO(004) peaks and no other phases within the scan range [Fig. 1(c)]. A clearly separable CFO(004) [the inset, Fig. 1(c)] peak gives a perpendicular lattice constant of 8.365 Å, indicating a CFO film under slight tensile strain compared to bulk CFO lattice constant of 8.392 Å [17]. Finally, a cross-sectional HAADF STEM image shows an atomically sharp interface between the MgO substrate and the CFO thin film with an epitaxial relationship of $[100]_{\mathrm{MgO}}\|[100]_{\mathrm{CFO}}$ and $[010]_{\mathrm{MgO}}\|[010]_{\mathrm{CFO}}$ as indicated in Fig. 1(d). The appearance of the lattice varies across the CFO thin film, switching between a cubic appearance and that which resembles a spinel structure. We believe this contrast variation is due to changes in the degree of inversion λ. In $AB_2\mathrm{O}_4$ spinels, λ adopts values between 0 (normal) and 1 (inverse) and is equal to the fractional occupancy of the trivalent B^{3+} cation on the tetrahedral A-site sublattice. Figure 1(e) shows the Pt/CFO interface (see the Supplemental Material [25] for details).

Bulk magnetic properties of a Pt(1.7-nm)/CFO(40-nm) sample are measured at 5 K by vibrating sample magnetometry (VSM) [Fig. 1(f)]. An in-plane hysteresis loop taken along the [100] axis is shown as a red dashed line, whereas an out-of-plane hysteresis loop is shown as a black solid line. At temperatures below 50 K, MgO substrates contribute a paramagnetic background to the VSM signal, which has not been subtracted from the data. CFO samples which were not capped with Pt showed virtually identical magnetization characteristics.

To detect the MPE in Pt/CFO, we perform magnetotransport measurements that are sensitive to the presence of magnetization within the Pt layer. In ferromagnets, two well-known phenomena are the AHE, which is sensitive to the out-of-plane magnetization, and the AMR, which is sensitive to the orientation of magnetization relative to the current direction. With induced magnetization in the Pt layer along unit vector $\mathbf{m}_{\mathrm{Pt}}$, these appear in the longitudinal and transverse resistivities as [26]

$$\begin{aligned} \rho_{\mathrm{xx}} &= \rho_0 + \Delta\rho_{\mathrm{AMR}}\mathbf{m}_{\mathrm{Pt,j}}^2, \\ \rho_{\mathrm{xy}} &= \Delta\rho_{\mathrm{AMR}}\mathbf{m}_{\mathrm{Pt,t}}\mathbf{m}_{\mathrm{Pt,j}} + \rho_{\mathrm{AHE}}\mathbf{m}_{\mathrm{Pt,n}}, \end{aligned} \tag{1}$$

where $\mathbf{m}_{\mathrm{Pt,n}}$, $\mathbf{m}_{\mathrm{Pt,jt}}$, and $\mathbf{m}_{\mathrm{Pt,t}}$ are the out-of-plane (**n**), the in-plane along current (**j**), and in-plane transverse to current (**t**) components of the Pt magnetization unit vector [see Fig. 2(a)], ρ_0 is the background resistivity of Pt, and $\Delta\rho_{\mathrm{AMR}}$ and ρ_{AHE} are the MPE-induced AMR and AHE, respectively. In addition to AHE and AMR, a recently discovered pure spin current effect based on the spin Hall effect in Pt and interfacial spin scattering at the FMI interface generates additional contributions to ρ_{xx} and ρ_{xy} given by [27,28]

$$\begin{aligned} \rho_{\mathrm{xx}} &= \rho_0 + \Delta\rho_1\mathbf{m}_{\mathrm{CFO,t}}^2, \\ \rho_{\mathrm{xy}} &= -\Delta\rho_1\mathbf{m}_{\mathrm{CFO,t}}\mathbf{m}_{\mathrm{CFO,j}} + \Delta\rho_2\mathbf{m}_{\mathrm{CFO,n}}, \end{aligned} \tag{2}$$

where $\mathbf{m}_{\mathrm{CFO,j}}$, $\mathbf{m}_{\mathrm{CFO,t}}$, and $\mathbf{m}_{\mathrm{CFO,n}}$ are components of the magnetization unit vector in the FMI, $\Delta\rho_1$ is known as the SMR, and $\Delta\rho_2$ is the spin Hall anomalous Hall-like signal (SH-AHE). The SMR stems from the reflection of the spin current (generated by the spin Hall effect) from the FMI interface, which subsequently is converted to a charge current through the inverse spin Hall effect (ISHE) [27,28]. The SH-AHE stems from the reflection of the spin current at the FMI interface where an out-of-plane component of FMI magnetization rotates the spin orientation of the spin current and generates a transverse voltage via the ISHE. Finally, in

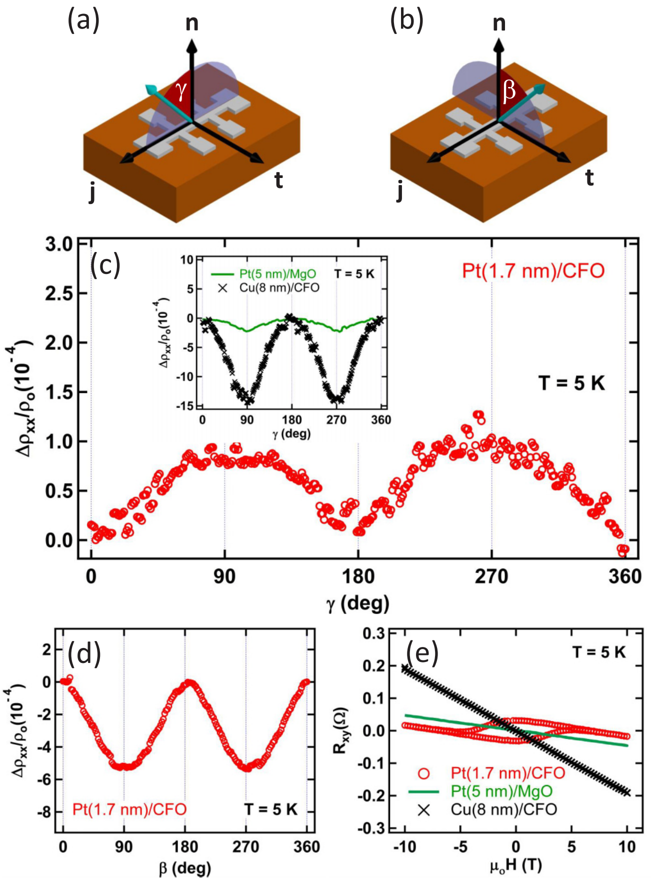

FIG. 2. (a) Measurement geometry for the AMR (γ scan on the n-j plane). (b) Measurement geometry for the SMR (β scan on the n-t plane). (c) γ dependence of $\Delta\rho_{\mathrm{xx}}/\rho_0$ of Pt/CFO taken with $\mu_0 H = 10$ T, showing the presence of the AMR. Inset: γ dependence of $\Delta\rho_{xx}/\rho_0$ of Pt/MgO (the green line) and Cu/CFO (the black crosses), showing OMR. (d) β dependence of $\Delta\rho_{\mathrm{xx}}/\rho_0$ of Pt/CFO taken with $\mu_0 H = 10$ T, showing the presence of the SMR. (e) Hall resistance for Pt(1.7 nm)/CFO (the red circles), Pt(5 nm)/MgO (the green line), and Cu(8 nm)/CFO (the black crosses). All measurements are taken at $T = 5$ K.

addition to the AMR and SMR effects, one also must consider the ordinary magnetoresistance (OMR) and ordinary Hall effect (OHE) that occur due to the presence of Lorentz forces acting on charge carriers in a magnetic field.

We begin with ADMR measurements to separate the contributions from the AMR, SMR, and OMR (see the Supplemental Material [25] for details). Considering that the AMR depends on the j component of magnetization [Eq. (1)] and the SMR depends on the t component of magnetization [Eq. (2)], the two effects can be separated by rotating the magnetization within different planes. For the AMR, the relevant angular scan is on the n-j plane, where γ is defined as the angle measured from the normal axis (n) [see Fig. 2(a)] whereas the SMR does not depend on γ. For the SMR, the relevant angular scan is on the n-t plane, where β is defined as the angle measured from the normal axis (n) [see Fig. 2(b)] whereas the AMR does not depend on β. Finally, the contribution from the OMR has the same functional form as the AMR (i.e., depends on γ), although the OMR can be determined independently. The OMR in most materials has a higher resistance when the magnetic field is perpendicular to the current ($\gamma = 0^\circ$) as compared to parallel to the current ($\gamma = 90^\circ$), and we have verified this for our Pt films on MgO(001) substrates as well [the inset in Fig. 2(c)]. To determine if the Pt/CFO system exhibits a MPE, we therefore perform a γ scan to look for the presence of the AMR in a fixed field of 10 T. Figure 2(c) clearly shows the presence of ADMR with lower resistivity for $\gamma = 0^\circ$ and higher resistivity for $\gamma = 90^\circ$. Because this cannot be explained by the OMR (opposite polarity) and the γ scan is insensitive to the SMR, it is clear evidence for the AMR and induced ferromagnetism in the Pt layer. By comparison, the Fig. 2(c) inset shows γ scans of Pt/MgO and Cu/CFO with both displaying OMR oscillations [note that we used a thicker (8-nm) Cu layer since 1.7-nm films ended up having very high-resistivity values]. This is the strongest evidence for the MPE in Pt/CFO in our Rapid Communication. Such an AMR signature has been reported previously for other Pt/FMI systems and is accepted as the most reliable test among transport measurements for the MPE [10,26,27]. Finally, a β scan shows a SMR with a magnitude similar to previously reported studies [11–13,15] of Pt/CoFe$_2$O$_4$ [Fig. 2(d)].

We also perform Hall measurements to further support the presence of induced ferromagnetism in the Pt layer. The measurement of R_{xy} at 5 K for the Pt(1.7-nm)/CFO(40-nm) sample [Fig. 2(e), the red circles] exhibits a nonlinear hysteretic signal commonly associated with the AHE (and thus ferromagnetism) and a linear OHE background. The absence of such nonlinear features in Cu(8-nm)/CFO(40-nm) and Pt(5-nm)/MgO control samples rule out magnetic fringe fields of the CFO or magnetic impurities in Pt, respectively, as the origin of the hysteresis loop in the Pt/CFO sample. It is interesting to note that after the linear OHE contribution is subtracted [Fig. 3(a), the red circles], the remaining hysteretic signal of Pt/CFO shows higher coercivity and a substantially larger remanence ratio than the out-of-plane hysteresis loop of bulk CFO [Fig. 1(f)]. This suggests an induced magnetic anisotropy inside the Pt layer which differs from the one seen in bulk CFO, although the precise microscopic mechanism causing the enhanced coercivity is unclear.

The Hall resistivity in Fig. 3(a) has contributions from the MPE-AHE and the SH-AHE. To separate these effects, we utilize a 2-nm Cu spacer which cannot have induced ferromagnetism (filled d shell) and is transparent to spin currents. Therefore, in Pt/Cu/CFO, the MPE-AHE should be blocked while the SH-AHE is maintained. The Hall measurement of Pt/Cu/CFO [Fig. 3(a), the blue line] indeed shows a reduction in magnitude compared to Pt/CFO, which indicates a loss of induced ferromagnetism and the MPE-AHE contribution. To isolate the spin Hall effect, we compare the SMR β scans of Pt/Cu/CFO and Pt/CFO [Fig. 3(b)]. The similar values of the SMR indicate that the spin Hall effect is maintained. Finally, a comparison of the AMR γ scans of Pt/Cu/CFO and Pt/CFO shows that the Cu layer reduces the AMR [Fig. 3(c)]. These studies indicate that the reduction in AHE in Pt/Cu/CFO is primarily due to the reduction of induced ferromagnetism.

Finally, we investigate the MPE in Pt/CFO using density functional theory calculations. Using the Vienna *ab initio* simulation package, we relax cubic CFO cells consisting of 5 f.u. (where f.u. represents formula units) with the Co atoms

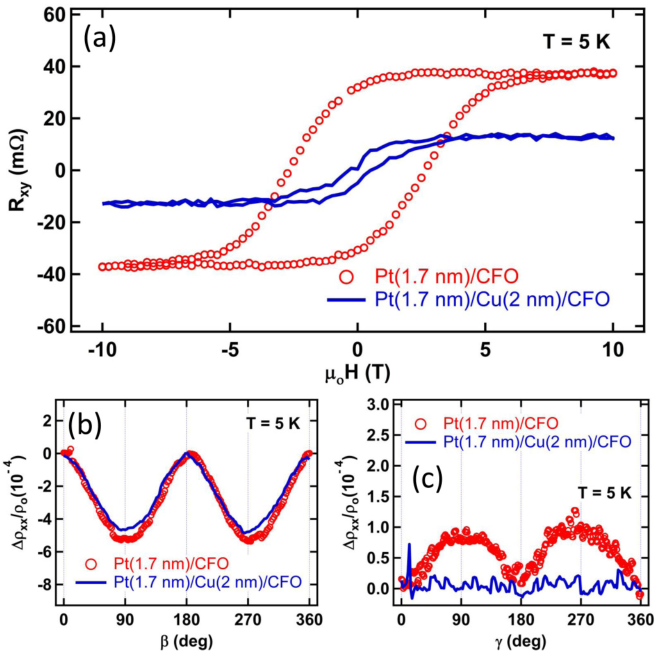

FIG. 3. (a) Hall resistivity of Pt(1.7 nm)/CFO (the red circles) and Pt(1.7 nm)/Cu(2 nm)/CFO (the blue line) with a linear OHE background subtracted. Addition of the Cu spacer heavily suppresses the magnitude and coercivity. (b) The SMR β scans of Pt/CFO (the red circles) and Pt/Cu/CFO (the blue line), (c) The AMR γ scans of Pt/CFO (the red circles) and Pt/Cu/CFO (the blue line). All measurements are taken at $T = 5$ K. The magnetic field was fixed at 10 T for the γ and β scans.

placed only on the tetrahedral sites, ordered octahedral sites, random octahedral sites, and a combination of random tetrahedral and octahedral sites [29]. These calculations indicate CFO favors Co occupancy of the octahedral sites to minimize the structural energy with random distribution and no preference for ordering. Using the lowest-energy CFO structure, we construct calculation cells consisting of either one or two cubic CFO cells topped with either four (~1-nm) or eight (~2-nm) layers of Pt with an (001)/(001) interface and at least 10 Å of vacuum. After comparing several Pt positions over the CFO cells, the positions directly over the cation sites are found to be energetically favorable as shown in Fig. 4(b). Finally, we relax the interface calculation cells on the plane of the interface to determine the electronic and magnetic structures of the CFO/Pt interface. All calculations are performed using generalized gradient approximation pseudopotentials in the formulation of Perdew *et al.*; on-site corrections for Coulomb interactions (DFT + U) are applied based on previous DFT work [30,31]. Calculations utilize spin polarization and Monkhorst-Pack k-point meshes consisting of seven points in the periodic directions and a single point in the vacuum directions.

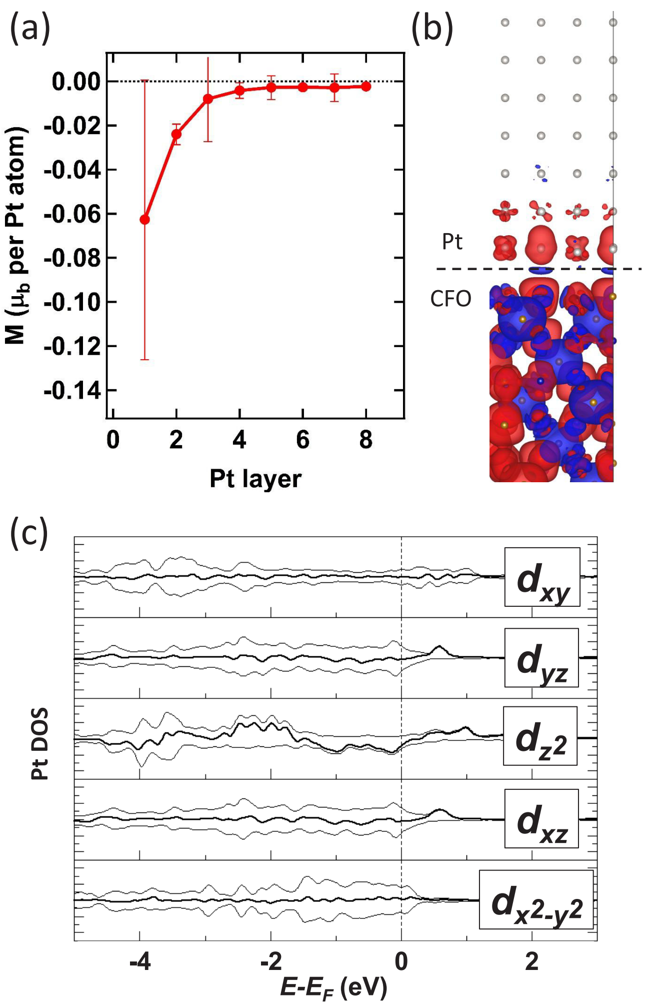

FIG. 4. (a) Average magnetic moment per Pt atom in μ_B for Pt layers adjacent to the CFO/Pt(001)/(001) interface, calculated with DFT. Layer averages decrease sharply to zero in one to two layers from the interface. (b) The magnetic moment isosurfaces at $0.0025\mu_B$ for the Pt atoms in the eight-layer calculation cell. Strong negative moments (red) are observed only in the layers closest to the interface, diminishing to zero by the fourth layer of the Pt atoms. (c) Orbital-resolved d-DOS of a Pt atom located directly over a magnetic Fe atom at the CFO/Pt interface. The thin lines are spin-up (positive values) and spin-down (negative values) DOS, and the bold line is their sum.

Figure 4(a) displays the layer-averaged magnetic moments on Pt atoms in layers adjacent to the CFO/Pt interface. The large error bars in the interface layer come from site-specific variations between the Pt atoms that we will discuss in the Supplemental Material [25]. We observe a decreasing moment on the Pt atoms as a function of distance from the CFO/Pt interface, indicating that the presence of the Pt moments should be due to induced magnetism from the CFO substrate. The magnetic effect does not persist after the first two Pt planes, giving a length scale for the proximity effect. Figure 4(b) displays the magnetic moments on the Pt atoms in the eight-layer calculation cell with isosurfaces at 0.0025 μ_B, showing that the induced negative moments (red) are only present on the first few atomic planes. To investigate the nature of the induced moments at the interface, we examine the orbital density of states of interfacial Pt atoms on top of various CFO sites (e.g., octahedral Fe, tetrahedral Fe, oxygen, and octahedral Co). In particular, as shown in Fig. 4(c), we observe a strong spin asymmetry (the bold line) and induced moment in the density of states of the dz^2 orbitals of Pt on top of octahedral Fe, whereas the other orbitals show much less spin asymmetry. Furthermore, a comparison with the *d*-DOS of Pt on top of the other CFO sites and an examination of the *d*-DOS of Fe suggest that magnetism is primarily induced in the dz^2 orbital of the Pt atoms by moments in the *dxy*, *dyz*, and *dxz* orbitals of the Fe atoms located no more than one layer below the CFO/Pt interface (see the Supplemental Material [25] for details).

In conclusion, we obtain strong evidence for the presence of induced ferromagnetism (i.e., the MPE) in Pt/CFO at 5 K including the first measurement of the AMR in this system. Studies of Hall resistivity, SMR, insertion of Cu spacers, and DFT calculations provide additional evidence for the MPE. Additional measurements indicate that the MPE at 300 K is likely based on the Hall signal, but the results are less conclusive than at 5 K because the angle-dependent γ scan has negative polarity (see the Supplemental Material [25]). The observation of the MPE in Pt/CFO opens the door to utilizing the family of spinel ferrites for the MPE and spin manipulation via proximity exchange fields for novel spintronic devices.

ACKNOWLEDGMENTS

We would like to thank F. Casanova for insightful discussions. Primary funding for this research was provided by the Center for Emergent Materials: an NSF MRSEC under Award No. DMR-1420451. N.A. and W.W. acknowledge computational support by the Ohio Supercomputer Center under Grant No. PAS0072 and partial funding from AFOSR, Award No. FA9550-14-1-0322.

W.A. and I.V.P. contributed equally to this work.

---

[1] H. Haugen, D. Huertas-Hernando, and A. Brataas, Phys. Rev. B **77**, 115406 (2008).

[2] H. X. Yang, A. Hallal, D. Terrade, X. Waintal, S. Roche, and M. Chshiev, Phys. Rev. Lett. **110**, 046603 (2013).

[3] S. Singh, J. Katoch, T. Zhu, K.-Y. Meng, T. Liu, J. T. Brangham, F. Yang, M. E. Flatté, and R. K. Kawakami, Phys. Rev. Lett. **118**, 187201 (2017).

[4] J. C. Leutenantsmeyer, A. A. Kaverzin, M. Wojtaszek, and B. J. van Wees, 2D Mater. **4**, 014001 (2017).

[5] P. Wei, S. Lee, F. Lemaitre, L. Pinel, D. Cutaia, W. Cha, F. Katmis, Y. Zhu, D. Heiman, J. Hone, J. S. Moodera, and C.-T. Chen, Nat. Mater. **15**, 711 (2016).

[6] C. Zhao, T. Norden, P. Zhang, P. Zhao, Y. Cheng, F. Sun, J. P. Parry, P. Taheri, J. Wang, Y. Yang, T. Scrace, K. Kang, S. Yang, G.-X. Miao, R. Sabirianov, G. Kioseoglou, W. Huang, A. Petrou, and H. Zeng, Nat. Nanotechnol. **12**, 757 (2017).

[7] Z. Wang, C. Tang, R. Sachs, Y. Barlas, and J. Shi, Phys. Rev. Lett. **114**, 016603 (2015).

[8] I. Vobornik, U. Manju, J. Fujii, F. Borgatti, P. Torelli, D. Krizmancic, Y. S. Hor, R. J. Cava, and G. Panaccione, Nano Lett. **11**, 4079 (2011).

[9] C. Tang, C.-Z. Chang, G. Zhao, Y. Liu, Z. Jiang, C.-X. Liu, M. R. McCartney, D. J. Smith, T. Chen, J. S. Moodera, and J. Shi, Sci. Adv. **3**, e1700307 (2017).

[10] C. Tang, P. Sellappan, Y. Liu, Y. Xu, J. E. Garay, and J. Shi, Phys. Rev. B **94**, 140403 (2016).

[11] M. Isasa, A. Bedoya-Pinto, S. Vélez, F. Golmar, F. Sánchez, L. E. Hueso, J. Fontcuberta, and F. Casanova, Appl. Phys. Lett. **105**, 142402 (2014).

[12] M. Valvidares, N. Dix, M. Isasa, K. Ollefs, F. Wilhelm, A. Rogalev, F. Sánchez, E. Pellegrin, A. Bedoya-Pinto, P. Gargiani, L. E. Hueso, F. Casanova, and J. Fontcuberta, Phys. Rev. B **93**, 214415 (2016).

[13] M. Isasa, S. Vélez, E. Sagasta, A. Bedoya-Pinto, N. Dix, F. Sánchez, L. E. Hueso, J. Fontcuberta, and F. Casanova, Phys. Rev. Appl. **6**, 034007 (2016).

[14] H. Wu, Q. Zhang, C. Wan, S. Ali, L. You, J. Wang, Y. Choi, and X. Han, IEEE Trans. Mag. **51**, 4100104 (2015).

[15] T. Tainosho, T. Niizeki, J.-i. Inoue, S. Sharmin, E. Kita, and H. Yanagihara, AIP Adv. **7**, 055936 (2017).

[16] Y. Suzuki, G. Hu, R. B. van Dover, and R. J. Cava, J. Magn. Magn. Mater. **191**, 1 (1999).

[17] G. Hu, J. H. Choi, C. B. Eom, V. G. Harris, and Y. Suzuki, Phys. Rev. B **62**, 779(R) (2000).

[18] H. Yanagihara, K. Uwabo, M. Minagawa, E. Kita, and N. Hirota, J. Appl. Phys. **109**, 07C122 (2011).

[19] S. F. Rus, A. Herklotz, R. Roth, L. Schultz, and K. Dörr, J. Appl. Phys. **114**, 043913 (2013).

[20] X. Chen, X. Zhu, W. Xiao, G. Liu, Y. P. Feng, J. Ding, and R.-W. Li, ACS Nano **9**, 4210 (2015).

[21] A. V. Ramos, Ph.D. Thesis, Universite Pierre et Marie Curie, 2009.

[22] A. V. Ramos, M.-J. Guittet, and J.-B. Moussy, Appl. Phys. Lett. **91**, 122107 (2007).

[23] M. Jean-Baptiste, J. Phys. D: Appl. Phys. **46**, 143001 (2013).

[24] T. Kuschel, C. Klewe, J. M. Schmalhorst, F. Bertram, O. Kuschel, T. Schemme, J. Wollschläger, S. Francoual, J. Strempfer, A. Gupta, M. Meinert, G. Götz, D. Meier, and G. Reiss, Phys. Rev. Lett. **115**, 097401 (2015).

[25] See Supplemental Material at http://link.aps.org/supplemental/10.1103/PhysRevMaterials.2.011401 for details of the experimental methods (material synthesis and magnetotransport measurements), characterization of the Pt/CoFe$_2$O$_4$ interface, magnetotransport measurements at room temperature, and the orbital density of states DFT calculation.

[26] X. Zhou, L. Ma, Z. Shi, W. J. Fan, J.-G. Zheng, R. F. L. Evans, and S. M. Zhou, Phys. Rev. B **92**, 060402 (2015).

[27] Y.-T. Chen, S. Takahashi, H. Nakayama, M. Althammer, S. T. B. Goennenwein, E. Saitoh, and G. E. W. Bauer, Phys. Rev. B **87**, 144411 (2013).

[28] H. Nakayama, M. Althammer, Y. T. Chen, K. Uchida, Y. Kajiwara, D. Kikuchi, T. Ohtani, S. Geprägs, M. Opel, S. Takahashi, R. Gross, G. E. W. Bauer, S. T. B. Goennenwein, and E. Saitoh, Phys. Rev. Lett. **110**, 206601 (2013).

[29] G. Kresse and J. Furthmüller, Phys. Rev. B **54**, 11169 (1996).

[30] J. P. Perdew, K. Burke, and M. Ernzerhof, Phys. Rev. Lett. **77**, 3865 (1996).

[31] A. Walsh, S.-H. Wei, Y. Yan, M. M. Al-Jassim, J. A. Turner, M. Woodhouse, and B. A. Parkinson, Phys. Rev. B **76**, 165119 (2007).